Supporting Information

N/O Co-Doped Porous Carbon Derived from Polyester Waste for Electrochemical Production of H_2O_2

Mingsheng Luo, [a] Chupeng Wang, [a] Shiqi Song, [a] Maochong Tang, [a] Xiao Xia Wang, *[b] Min Wu [c]

[a] School of Materials Science and Engineering, East China University of Science and Technology, Shanghai 200237, China

[b] School of Mechanical and Power Engineering, East China University of Science and Technology, Shanghai 200237, China

[c] The Tibetan-Plateau Scientific Research Center of Lhasa, Lhasa 850000, China

* Correspondence: wangxiaoxia@ecust.edu.cn

Experimental Section

Materials

PET powder (50-74 μm) was obtained from Hengfa Plasticizing. Melamine and magnesium oxide (<30 nm) were purchased from Shanghai Dibo Biotechnology Co. Isopropanol (≥99.7%) was provided by Shanghai Titan Technology Co..Nafion solution was purchased from DuPont, and hydrochloric acid and sulfuric acid were from Sinopharm Chemical Reagent Co..

Synthesis of NOPC

Different mass ratios of MgO and PET (M/P=0.25, 0.5, 1, 2; where M refers to MgO and P to PET) were mixed and ground in an agate mortar for 10 minutes. The mixture was heated in a muffle furnace at a ramp rate of 5 °C min^{-1} up to 800 °C for 1 hour under N_2 atmosphere. The carbonation products were stirred in 1 M HCl for 8 hours to remove MgO. The samples were washed with deionized water to pH=7 and then dried in a vacuum oven at 70 °C for 10 hours. The obtained carbon materials were designated as OPC0.25-800, OPC0.5-800, OPC1-800, and OPC2-800, corresponding to different ratios. The mixture with the ratio of M/P=1 was also heated to 700 °C, 800 °C, 900 °C, and 1000 °C at a ramp rate of 5 °C min^{-1} for 1 hour under N_2 atmosphere. They were labeled as OPC1-700, OPC1-800, OPC1-900, and OPC1-1000, respectively.

Melamine was chosen as the nitrogen resource, which was mixed with MgO and PET at a mass ratio of 1:1:X (MgO: PET: melamine, where X = 0.05, 0.1, 0.3, 0.5). The mixtures were heated up to 300 °C at a rate of 5 °C min^{-1} for 10 min and then at 800 °C for 1 hour. The carbonation products were stirred in an acid solution with 1 M HCl and 2 M HNO_3 for 4 hours, then washed with deionized water to PH=7 and dried in a vacuum oven at 70 °C for 10 hours. The obtained carbon materials derived from different melamine additive amounts were recorded as NOPC-0.05, NOPC-0.1, NOPC-0.3, and NOPC-0.5, respectively.

Characterization

Fourier-transform infrared spectroscopy (FT-IR, Japan-Shimadzu-IR Tracer 100) was used to track chemical bond changes during low-temperature pre-treatment and pyrolysis. X-ray diffraction (XRD, Japan-Rigaku-Ultima IV) under Cu Kα radiation was employed to analyze the phase structure of the products. Raman spectroscopy (Japan-Horiba-Lab RAM HR Evolution) was used to quantify carbon defects. The morphology and structure of the synthesized samples were examined using field emission scanning electron microscopy (FESEM, JSM-IT800,20KV) and transmission electron microscopy (TEM, Talos F200X). The surface elemental composition and distribution of the catalysts were assessed through energy dispersive spectroscopy (EDS). Nitrogen adsorption-desorption isotherm at 77 K was obtained by Automatic Specific Surface and Porosity Analyzer (Micro meritics ASAP 2020). The mesopore volume was derived from nitrogen adsorption at a relative pressure of 0.984. Specific surface area and pore size distribution were evaluated by the Brunauer-Emmett-Teller (BET) equation and the Barrett-Joyner-Halenda (BJH) method. X-ray photoelectron spectroscopy (XPS, USA-ThermoFisher Nexsa) was applied to characterize the surface elemental composition, with N1s and C1s spectra analyzed via Advantage software. Thermogravimetric analysis (TGA, TGA 8000) was employed to evaluate the material degradation process and thermal stability.

Electrochemical Measurements

All electrochemical tests of the electrocatalysts were performed in a three-electrode system at room temperature through an electrochemical workstation (CHI760E) in acidic solution (0.5 M H_2SO_4). A carbon rod was used as a counter electrode, a saturated Hg/$HgSO_4$ electrode was used as a reference electrode, and a glassy carbon electrode (GCE, E7R9 RRDE) loaded with PET-derived carbon was used as a working electrode. Initially, the GCE was polished using 50 nm alumina powder, followed by ultrasonic cleaning in anhydrous ethanol and deionized water for 20 seconds. After that, the catalyst ink was applied onto the surface of the GCE. The catalyst ink was prepared by dispersing 5 mg of electrocatalyst in 1 mL of isopropanol with 15 μL of Nafion solution (5 wt%), which was ultrasonicated for 1 hour to ensure uniform dispersion. Subsequently, 10 μL of the ink was pipetted and dropped onto the cleaned glass carbon disk. The working electrode was dried at room temperature with a catalyst loading of 0.2 mg cm^{-2}. At first, Cyclic Voltammetry (CV) was performed at a scan rate of 50 mV s^{-1} for 20 cycles to obtain a stable CV response in N_2-saturated electrolyte. Then, CV and LSV tests were performed to evaluate the oxygen reduction activity of the catalyst in the oxygen (O_2)-saturated electrolyte. The potential on the Pt ring was maintained at 1.2 V relative to the reversible hydrogen electrode (RHE). The potential was converted to the reversible hydrogen electrode (RHE) using the following equation:

$$E_{RHE} = E\ (Hg_2SO_4)\ + 0.0591 * pH + 0.64(V) \tag{1}$$

The electron transfer number (n) and the selectivity of H_2O_2 were calculated from the polarization curves in the following equation:

$$n = \frac{4 * |I_D|}{|I_D| + |I_R|/N} \tag{2}$$

$$H_2O_2\% = 200 * \frac{|I_R|/N}{|I_D| + |I_R|/N} \tag{3}$$

Where I_D is the disk current, I_R the ring current, and N the collection efficiency of the RRDE, which was experimentally determined as 34.2% by the redox of Fe^{3+}/Fe^{2+} (Fig. S 1).

The kinetic current density was calculated according to the K-L equation:

$$\frac{1}{J} = \frac{1}{j_k} + \frac{1}{j_L} \tag{4}$$

$$j_L = 0.62nFC_0{D_0}^{2/3}v^{-1/6}\omega^{1/2} \tag{5}$$

Here, J is the measured current density, J_k and J_L are kinetic current density and limiting current density, respectively. n is the electron transfer number, F the Faraday constant (96485 C mol^{-1}), C_0 the oxygen concentration in solution (1.1×10^{-3} mol L^{-1} for 0.5 M H_2SO_4), D_0 the diffusion coefficient of oxygen (1.65×10^{-5} cm^2 s^{-1} for 0.5 M H_2SO_4), and v the kinematic viscosity of the solution (0.01 cm^2 s^{-1}).Finally, the electrochemical performance of the catalysts was evaluated using Tafel slope curves by the following equation:

$$\eta = b * log j_k + a \tag{6}$$

Where ŋ is the potential in LSV curves, and b the Tafel slope.

The electrochemical active surface area (ECSA) of the catalysts was estimated by the double-layer capacitance (C_{dl}), which was calculated according to the following formula:

$$C_{dl} = \frac{(J_a - J_c)}{2v} \tag{7}$$

Where j_a, and j_c are the capacitance current densities at 0.59 V in the positive and negative voltage scans, respectively. ν is the scan rate. CV scans were conducted at the potential window from 0.54 to 0.64 V with scan rates of 10, 20, 30, 40, and 50 mV s^{-1}.

The stability of the catalyst was characterized by an amperometric i-t curve in an acidic electrolyte saturated with O_2, where the disk voltage was fixed at 0.3 V (vs. RHE) and the ring voltage was fixed at 1.2 V (vs. RHE).

H_2O_2 production tests were conducted in an H-type electrolytic cell, utilizing Nafion 212 as a diaphragm. The catalyst (1.25 mg) was dispersed in a mixture of 1 mL isopropanol and 15 μL Nafion solution, then sonicated for 1 hour to form a stable catalyst ink. The ink was uniformly sprayed onto a 6.25 cm^2 carbon paper and subsequently dried under an infrared lamp. The working electrode was achieved with the catalyst loading of 0.2 mg cm^{-2}. The electrolyte in both the cathode and anode chambers of the cell was 20 mL of 0.5 M H_2SO_4. The electrolysis experiments were carried out under oxygen-saturated conditions using the amperometric i-t curve test. The concentration of H_2O_2 produced was determined by taking small amounts of the solution at 30 minutes intervals through the $Ce(SO_4)_2$ titration process with the following reaction equation:

$$2Ce^{4+} + H_2O_2 \rightarrow 2Ce^{3+} + 2H^+ + O_2\uparrow \tag{8}$$

The Faraday efficiency of the H_2O_2 production process was calculated by the following equation:

$$FE\% = \frac{2C_{H_2O_2} * V * F}{Q_{total}} \% \tag{9}$$

In the equation, Q_{total} was defined as the total charge (C) passed during the amperometric i-t curve test. $C_{H_2O_2}$ was referred to the concentration of H_2O_2 produced (mol L^{-1}). V was denoted as the volume of the electrolyte (L). F was the Faraday constant (96485 C mol^{-1}).

Supplementary Figures

The calibration of the collection efficiency was calibrated from one-electron reversible $[Fe(CN)_6]^{4-}$/ $[Fe(CN)_6]^{3-}$ system in an electrolyte of 10 mM $K_3[Fe(CN)_6]$ in 0.1 M KCL.

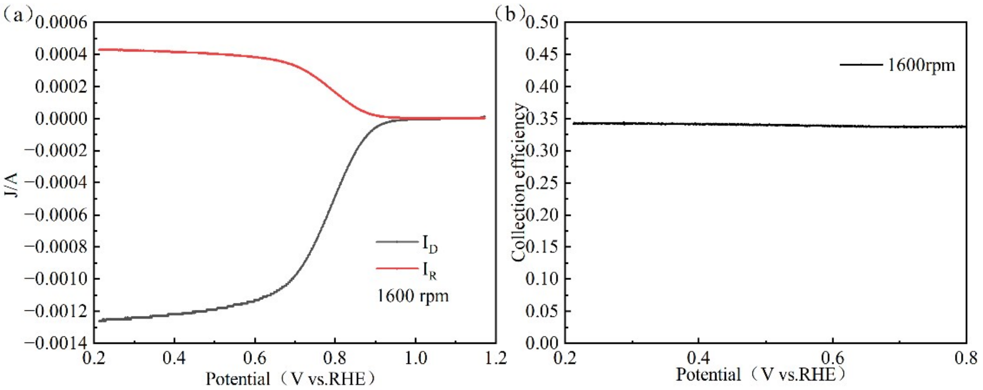

Fig. S 1 (a) RDE polarization curves for calibrating collection efficiency. (b) the collection efficiency N (34.2%) after calibration.

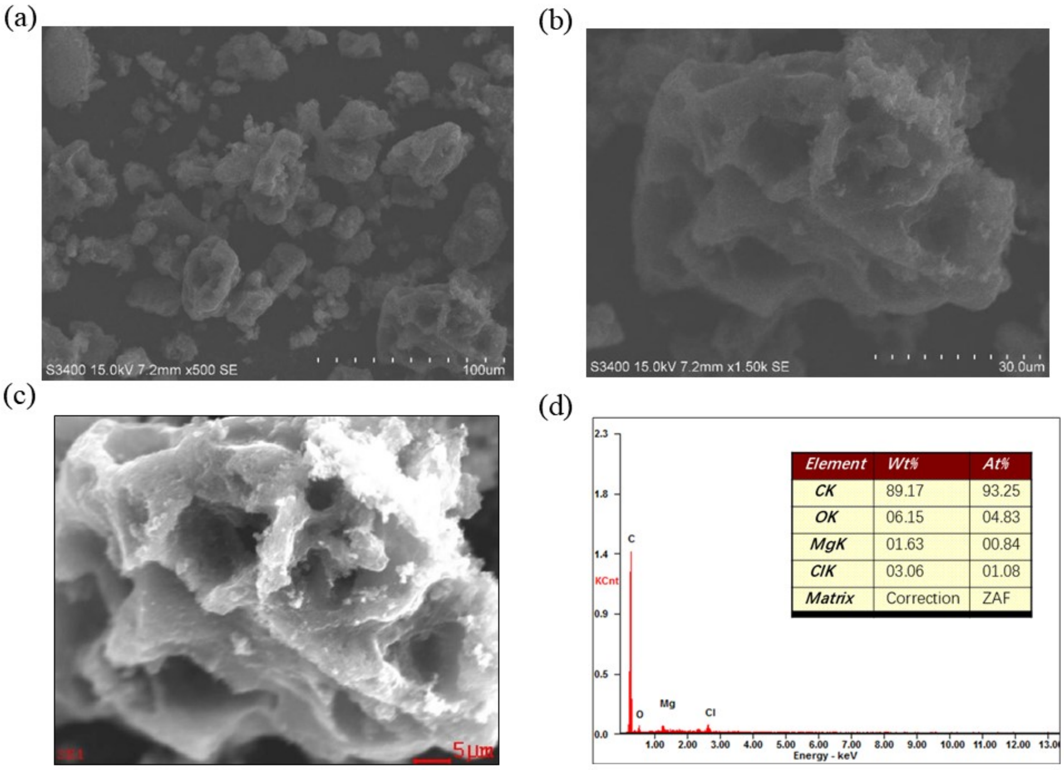

Element	Wt%	At%
CK	89.17	93.25
OK	06.15	04.83
MgK	01.63	00.84
ClK	03.06	01.08
Matrix	Correction	ZAF

Fig. S 2 SEM images (a-c) of OPC1-800, (d) EDS energy spectrum of (c).

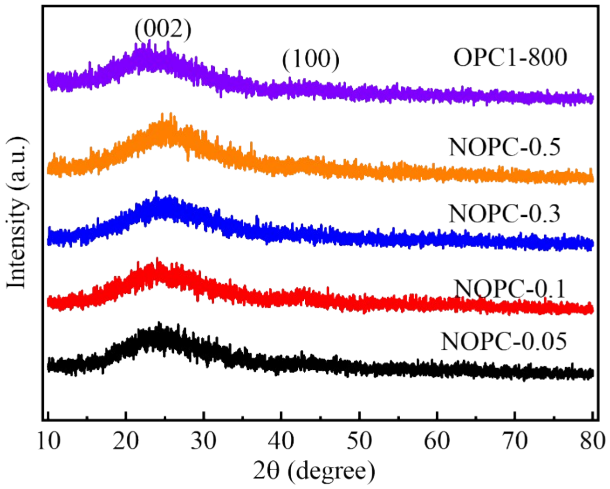

Fig. S 3 XRD patterns of different PET-derived carbon.

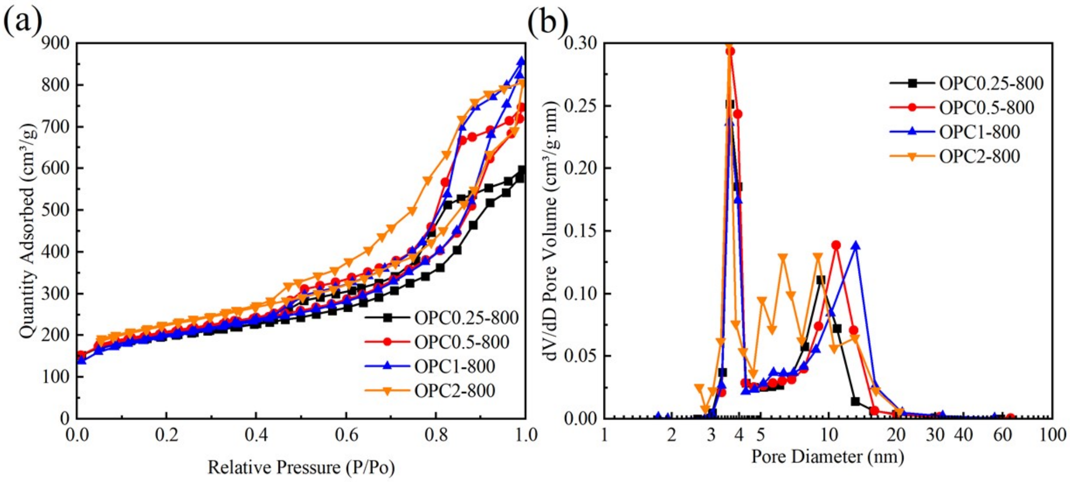

Fig. S 4 (a) N_2 adsorption-desorption isotherms and (b) pore size distribution by BJH method of different OPC samples.

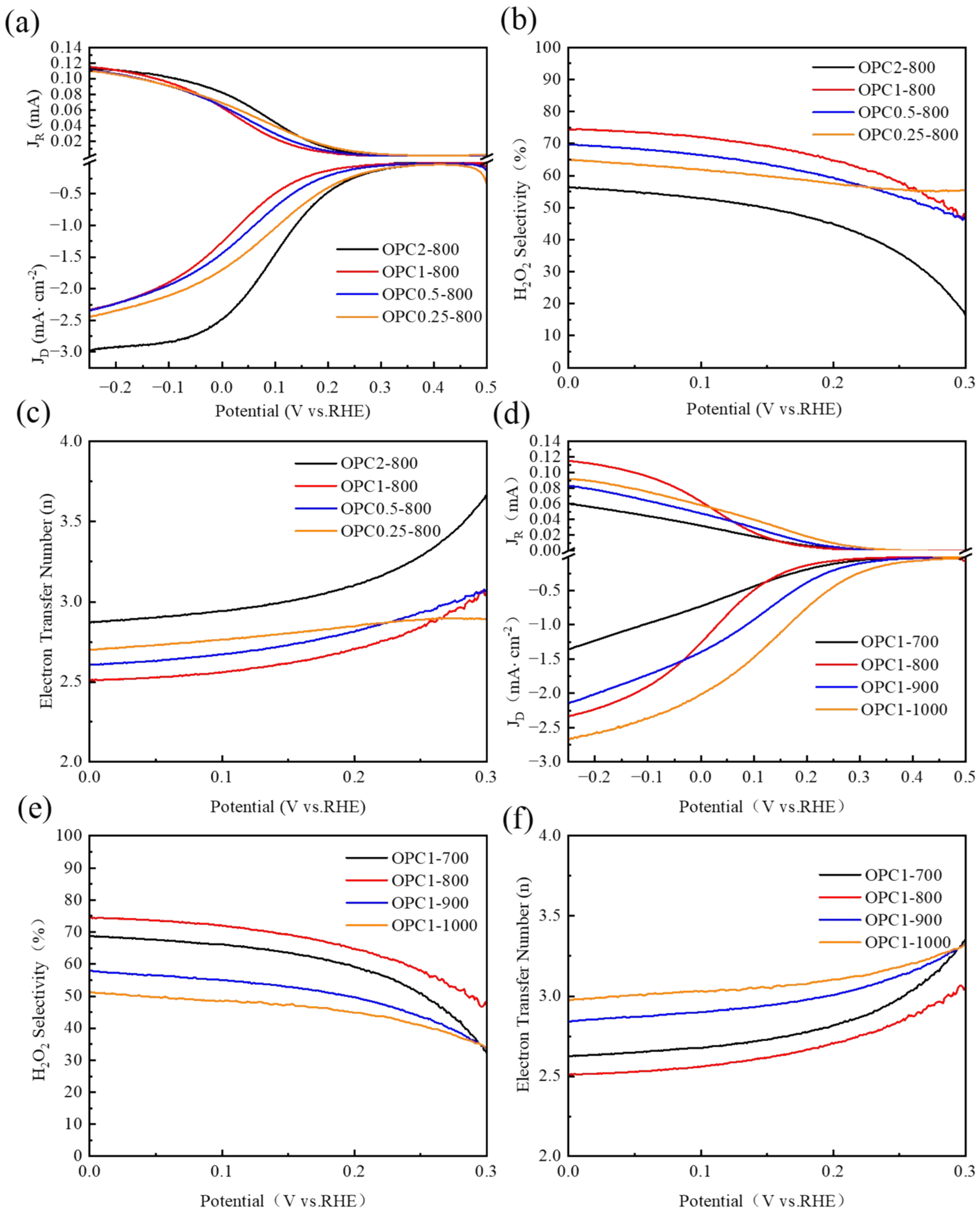

Fig. S 5. (a) LSV curves, (b) H_2O_2 selectivity, and (c) electron transfer number of the OPC samples. (d) LSV curves, (e) H_2O_2 selectivity, and (f) electron transfer number of the sample prepared at different carbonization temperatures with M/P=1.

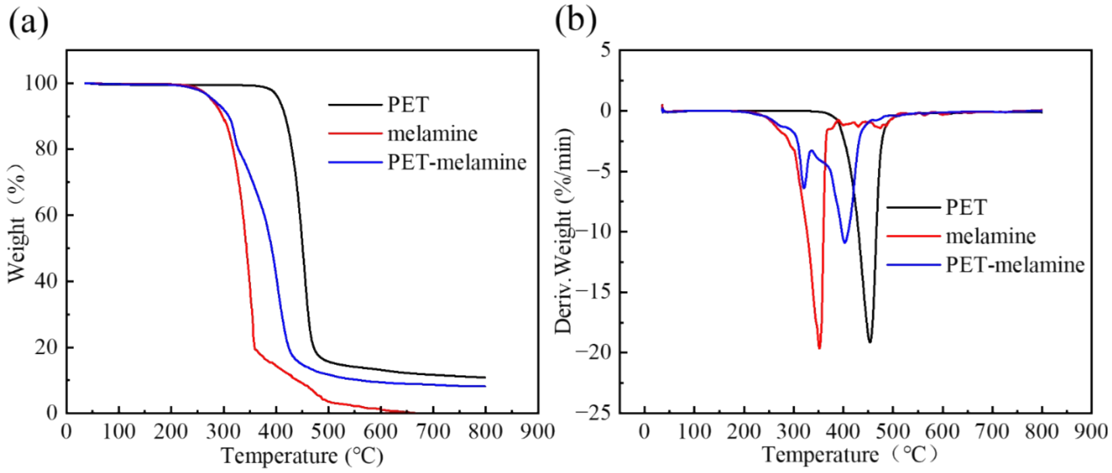

Fig. S 6. (a) TGA and (b) DTG curves for PET, melamine, and PET-melamine under a nitrogen environment.

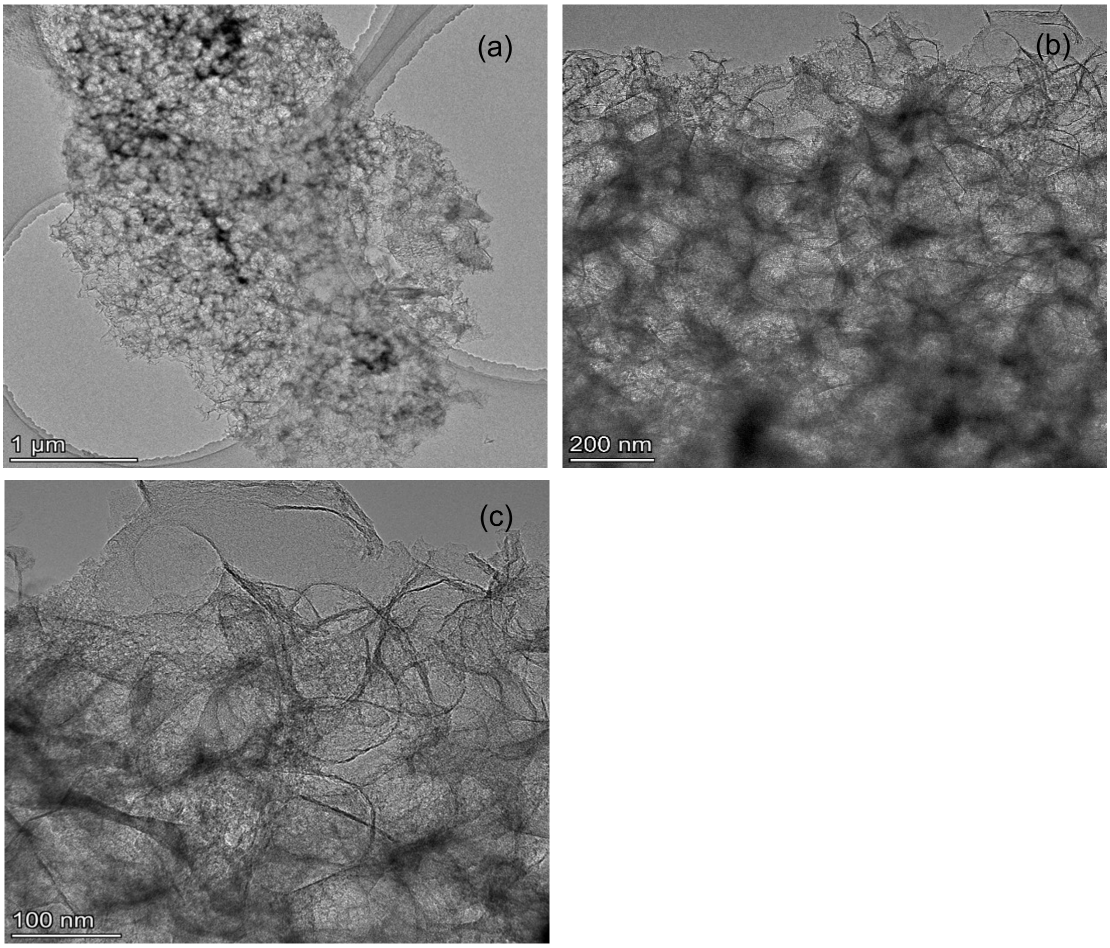

Fig. S 7. HRTEM images of NOPC-0.1.

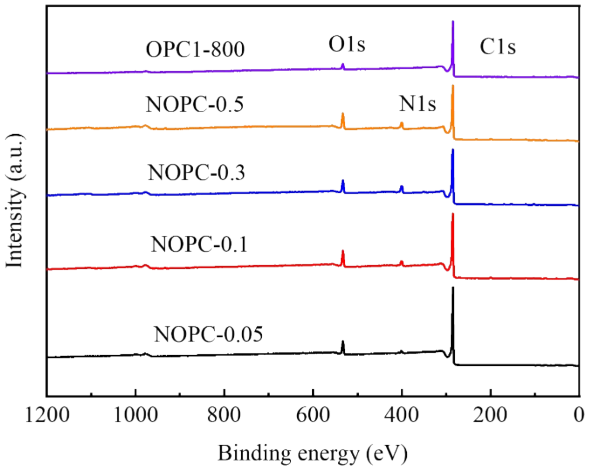

Fig. S 8. XPS spectra of OPC1-800, NOPC-0.05, NOPC-0.1, NOPC-0.3, and NOPC-0.5.

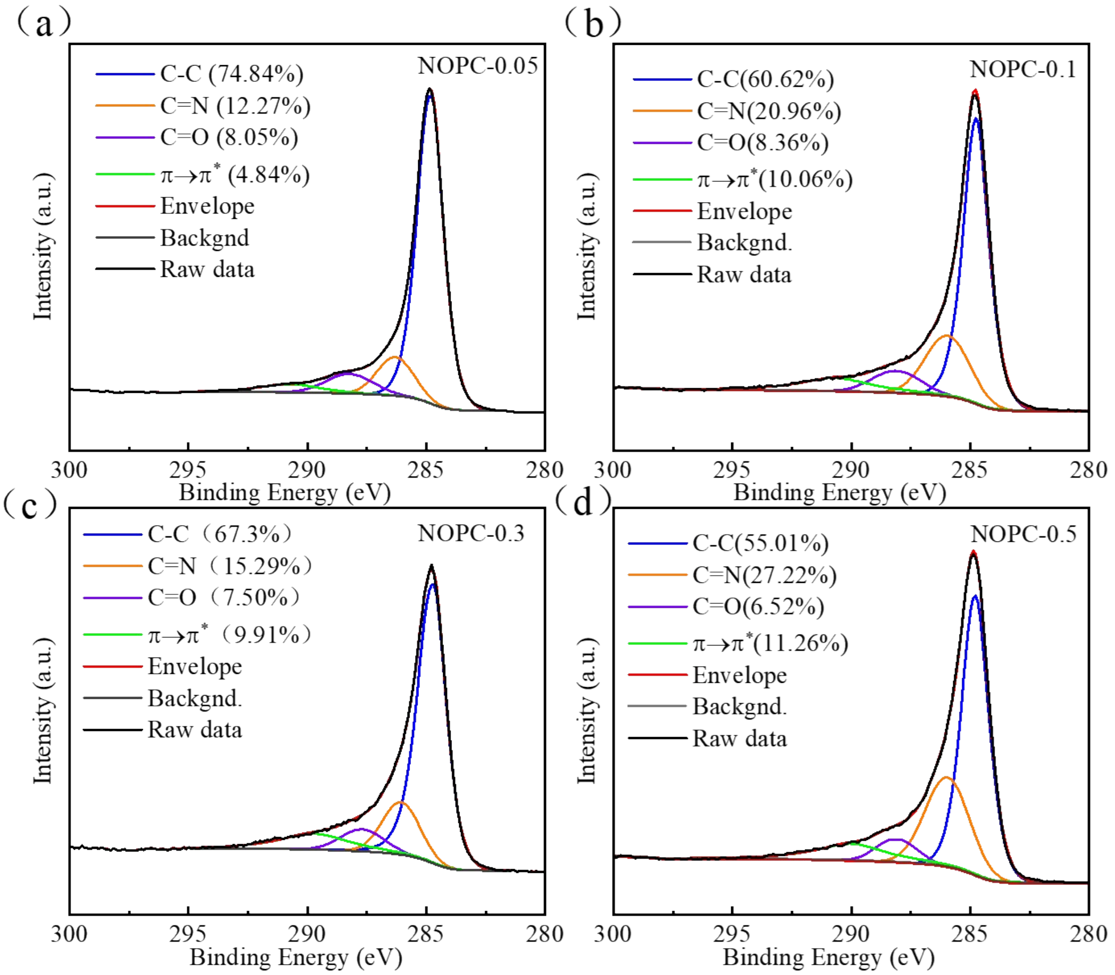

Fig. S 9. High-resolution C1s XPS spectra of different NOPC catalysts (a) NOPC-0.05, (b) NOPC-0.1, (c) NOPC-0.3, (d) NOPC-0.5.

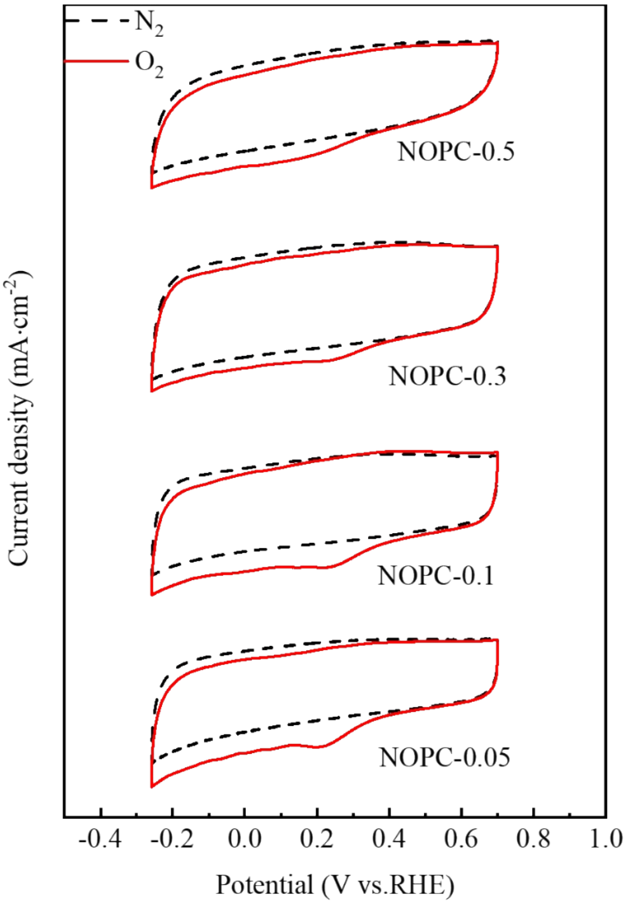

Fig. S 10. The CV curves of different NOPC samples under N_2 and O_2-saturated 0.5 M H_2SO_4.

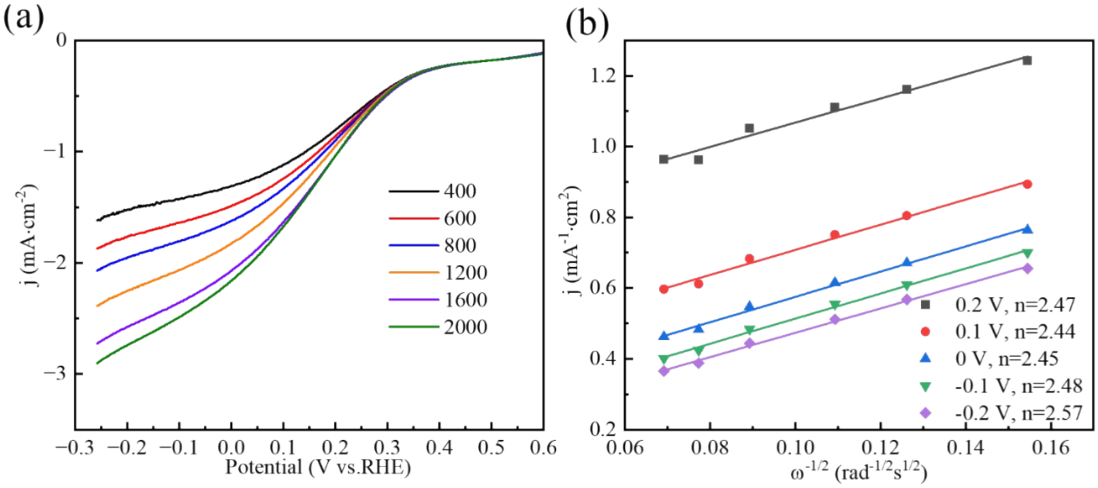

Fig. S 11. (a) LSV curves of NOPC-0.1 in O_2 saturated 0.5 M H_2SO_4 at different rotational speeds. (b) Koutecky-Levich plot of NOPC-0.1 based on the corresponding LSV curves.

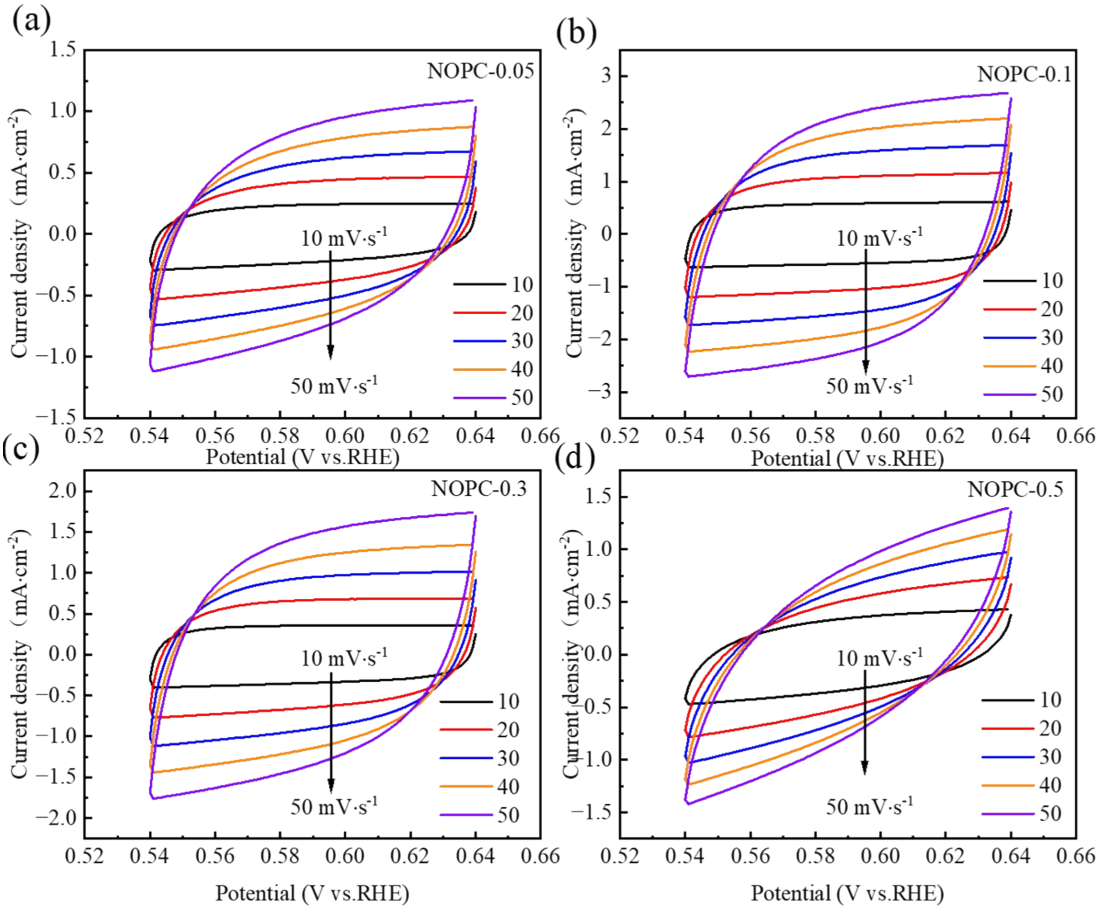

Fig. S 12. Cyclic voltammograms curves of (a) NOPC-0.05, (b) NOPC-0.1, (c) NOPC-0.3, and (d) NOPC-0.5 catalysts in the non-Faradaic potential region at scan rates of 10, 20, 30, 40, and 50 mV s^{-1} in 0.5 M H_2SO_4 electrolyte.

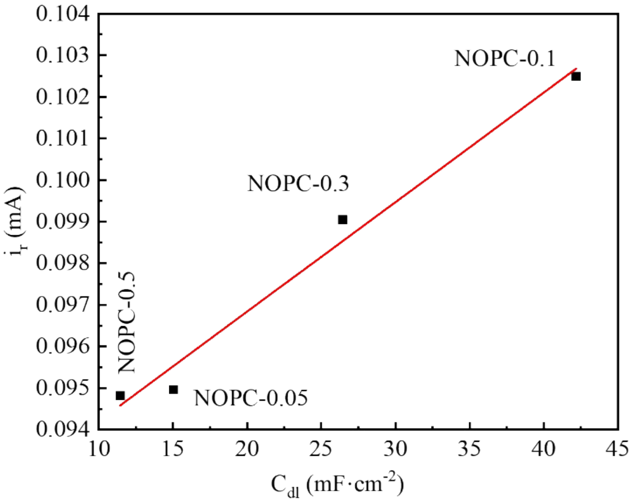

Fig. S 13. The relationship between the ring current at 0 V (vs. RHE) and the electrochemical double-layer capacitance of the NOPC catalysts.

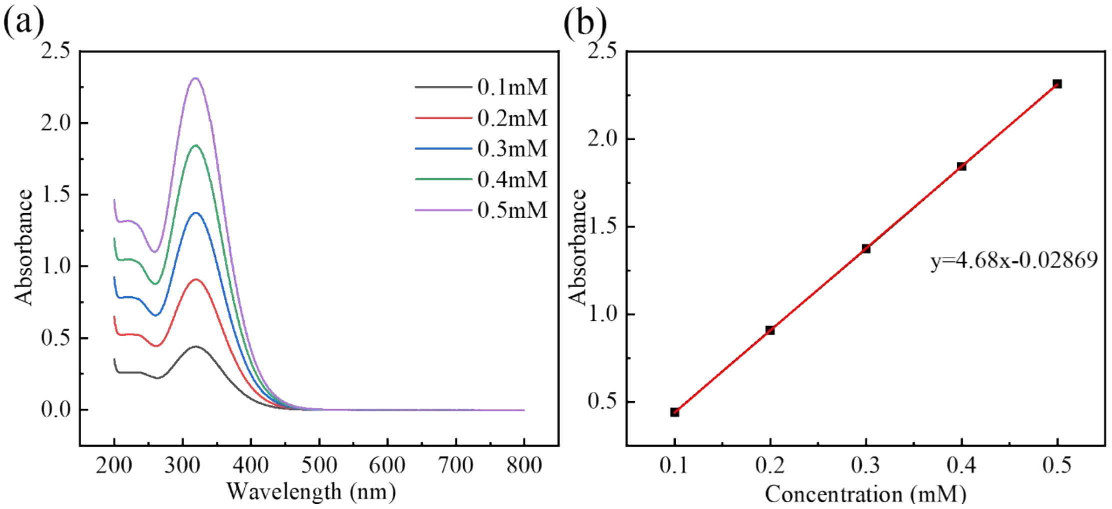

Fig. S 14. (a). UV-visible spectra of Ce^{4+} solution at different concentrations. (b) Standard curve corresponding to (a).

Table S1. The BET surface areas, micropore volumes, mesopore volumes, and average pore size of different samples.

Catalyst	BET(m^2g^{-1})	V_{mic}(cm^3g^{-1})	V_{mec}(cm^3g^{-1})	D_{pore}(nm)
PC-800	522.0548	0.228639	0.003579	2.8522
OPC0.25-800	720.6392	0.147740	0.777316	7.6453
OPC0.5-800	739.1882	0.132178	1.022351	8.3282
OPC1-800	696.9573	0.098571	1.223958	7.6088
OPC2-800	765.2493	0.129208	1.094052	7.2946
NOPC-0.05	409.2623	0.035214	1.372515	15.6250
NOPC-0.1	389.7711	0.059476	0.90447	13.7727
NOPC-0.3	718.8029	0.138707	0.538097	5.8556
NOPC-0.5	696.5098	0.135153	0.502305	5.7421

Table S2. Elemental content of different catalysts detected by XPS.

Sample	C(at%)	N(at%)	O(at%)
OPC1-800	95.19	0	4.31
NOPC-0.05	89.11	2.86	8.03
NOPC-0.1	85.58	5.15	9.27
NOPC-0.3	83.07	8.58	8.35
NOPC-0.5	81.17	7.64	11.19

Table S3. The N1s fitting results of XPS spectrum of different NOPC samples.

Sample	Peak BE (eV)	Atomic (%)	Nitrogen states
NOPC-0.05	398.67	27.97	Pyridinic N
	400.11	25.39	Pyrrolic N
	401.03	46.64	Graphitic N
NOPC-0.1	398.48	31.72	Pyridinic N
	400.11	29.18	Pyrrolic N
	401.03	28.41	Graphitic N
	403.53	10.70	N-oxide
NOPC -0.3	398.41	32.78	Pyridinic N
	399.93	26.82	Pyrrolic N
	400.95	31.62	Graphitic N
	403.81	8.78	N-oxide
NOPC -0.5	398.34	34.22	Pyridinic N
	399.82	20.11	Pyrrolic N
	400.77	36.47	Graphitic N
	403.17	9.20	N-oxide

Table S4. The C1s fitting results of the XPS spectrum of different NOPC samples

Sample	Peak BE (eV)	Atomic (%)	Carbon states
NOPC-0.05	284.80	74.84	C-C
	286.31	12.27	C=N
	288.23	8.05	C=O
	290.75	4.84	$\pi \rightarrow \pi^*$
NOPC-0.1	284.80	60.62	C-C
	286.00	20.96	C=N
	288.13	8.36	C=O
	290.73	10.06	$\pi \rightarrow \pi^*$
NOPC-0.3	284.80	67.30	C-C
	286.16	15.29	C=N
	287.78	7.50	C=O
	289.82	9.91	$\pi \rightarrow \pi^*$
NOPC-0.5	284.80	55.01	C-C
	285.96	27.22	C=N
	288.06	6.52	C=O
	290.03	11.26	$\pi \rightarrow \pi^*$

Table S5. Summary of previously reported catalysts in terms of their electrolyte and 2e⁻ ORR activity.

Catalyst	electrolyte	Selectivity (%)	Productivity (mmol g^{-1} h^{-1})	FE (%)	Stability（h）	Reference
NOPC	0.5M H_2SO_4	84.77	261.23	86.5	10	This Work
Co−SACs	0.1M $HClO_4$	>95	590	N/A	11	[1]
Co-N-C	0.5M H_2SO_4	80	N/A	N/A	N/A	[2]
p-PDA/XC	0.1M $HClO_4$	96	171	N/A	8	[3]
NCMK	0.5M H_2SO_4	95	157.5	70	6	[4]
NF-Cs	0.5 M H_2SO_4	93.1	N/A	85	2	[5]
Cationic covalent triazine network	0.1 M KOH	85.3	N/A	N/A	8	[6]
FPC-800	0.05M H_2SO_4	85	112.6	97.5	N/A	[7]
RF-AQ/Vulcan XC72	0.1 M H_2SO_4	85	N/A	70	24	[8]
B/N co-doped	0.1M KOH	85	N/A	N/A	50	[9]
p/N co-doped	0.1M KOH	80	223.4	80	4	[10]
NCC	0.5M H_2SO_4	80	N/A	N/A	N/A	[11]
Mo1/OSG-H	PBS (pH 8.7)	77	N/A	N/A	8	[12]
Mesoc	0.1 KOH	70%	N/A	N/A	N/A	[13]
MCHS	0.5M H_2SO_4	70	N/A	N/A	N/A	[14]
N/C-900	0.1 M KOH	56.67	N/A	39.54	N/A	[15]

References:

1. C. Tang, L. Chen, H. Li, L. Li, Y. Jiao, Y. Zheng, H. Xu, K. Davey and S. Z. Qiao, Tailoring Acidic Oxygen Reduction Selectivity on Single-Atom Catalysts via Modification of First and Second Coordination Spheres, *J Am Chem Soc*, 2021, **143**, 7819-7827.
2. Y. Sun, L. Silvioli, N. R. Sahraie, W. Ju, J. Li, A. Zitolo, S. Li, A. Bagger, L. Arnarson, X. Wang, T. Moeller, D. Bernsmeier, J. Rossmeisl, F. Jaouen and P. Strasser, Activity-Selectivity Trends in the Electrochemical Production of Hydrogen Peroxide over Single-Site Metal-Nitrogen-Carbon Catalysts, *J Am Chem Soc*, 2019, **141**, 12372-12381.
3. D. Wang, S. Li, X. Zhang, B. Feng, Y. Pei, Y. Zhu, W. Xu, Z.-H. Li, M. Qiao and B. Zong, Pyrolyzed polydopamine-modified carbon black for selective and durable electrocatalytic oxygen reduction to hydrogen peroxide in acidic medium, *Applied Catalysis B: Environmental*, 2022, **305**,121036-121047.
4. Y. Sun, I. Sinev, W. Ju, A. Bergmann, S. Dresp, S. Kühl, C. Spöri, H. Schmies, H. Wang, D. Bernsmeier, B. Paul, R. Schmack, R. Kraehnert, B. Roldan Cuenya and P. Strasser, Efficient Electrochemical Hydrogen Peroxide Production from Molecular Oxygen on Nitrogen-Doped Mesoporous Carbon Catalysts, *ACS Catalysis*, 2018, **8**, 2844-2856.
5. N. Jia, T. Yang, S. Shi, X. Chen, Z. An, Y. Chen, S. Yin and P. Chen, N,F-Codoped Carbon Nanocages: An Efficient Electrocatalyst for Hydrogen Peroxide Electroproduction in Alkaline and Acidic Solutions, *ACS Sustainable Chemistry & Engineering*, 2020, **8**, 2883-2891.
6. L. Z. Peng, P. Liu, Q. Q. Cheng, W. J. Hu, Y. A. Liu, J. S. Li, B. Jiang, X. S. Jia, H. Yang and K. Wen, Highly effective electrosynthesis of hydrogen peroxide from oxygen on a redox-active cationic covalent triazine network, *Chem Commun (Camb)*, 2018, **54**, 4433-4436.
7. K. Zhao, Y. Su, X. Quan, Y. Liu, S. Chen and H. Yu, Enhanced H2O2 production by selective electrochemical reduction of O2 on fluorine-doped hierarchically porous carbon, *Journal of Catalysis*, 2018, **357**, 118-126.
8. A. Wang, A. Bonakdarpour, D. P. Wilkinson and E. Gyenge, Novel organic redox catalyst for the electroreduction of oxygen to hydrogen peroxide, *Electrochimica Acta*, 2012, **66**, 222-229.
9. S. Chen, Z. Chen, S. Siahrostami, D. Higgins, D. Nordlund, D. Sokaras, T. R. Kim, Y. Liu, X. Yan, E. Nilsson, R. Sinclair, J. K. Norskov, T. F. Jaramillo and Z. Bao, Designing Boron Nitride Islands in Carbon Materials for Efficient Electrochemical Synthesis of Hydrogen Peroxide, *J Am Chem Soc*, 2018, **140**, 7851-7859.
10. Y. Sun, S. Li, B. Paul, L. Han and P. Strasser, Highly efficient electrochemical production of hydrogen peroxide over nitrogen and phosphorus dual-doped carbon nanosheet in alkaline medium, *Journal of Electroanalytical Chemistry*, 2021, **896**,115197-115203.
11. Y. Wu, A. Muthukrishnan, S. Nagata and Y. Nabae, Kinetic Understanding of the Reduction of Oxygen to Hydrogen Peroxide over an N-Doped Carbon Electrocatalyst, *The Journal of Physical Chemistry C*, 2019, **123**, 4590-4596.
12. C. Tang, Y. Jiao, B. Shi, J. N. Liu, Z. Xie, X. Chen, Q. Zhang and S. Z. Qiao, Coordination Tunes Selectivity: Two-Electron Oxygen Reduction on High-Loading Molybdenum Single-Atom Catalysts, *Angew Chem Int Ed Engl*, 2020, **59**, 9171-9176.
13. S. Chen, Z. Chen, S. Siahrostami, T. R. Kim, D. Nordlund, D. Sokaras, S. Nowak, J. W. F. To, D. Higgins, R. Sinclair, J. K. Nørskov, T. F. Jaramillo and Z. Bao, Defective Carbon-Based Materials for the Electrochemical Synthesis of Hydrogen Peroxide, *ACS Sustainable Chemistry & Engineering*, 2017, **6**, 311-317.

14. Y. Pang, K. Wang, H. Xie, Y. Sun, M.-M. Titirici and G.-L. Chai, Mesoporous Carbon Hollow Spheres as Efficient Electrocatalysts for Oxygen Reduction to Hydrogen Peroxide in Neutral Electrolytes, *ACS Catalysis*, 2020, **10**, 7434-7442.
15. Y. Yang, F. He, Y. Shen, X. Chen, H. Mei, S. Liu and Y. Zhang, A biomass derived N/C-catalyst for the electrochemical production of hydrogen peroxide, *Chem Commun (Camb)*, 2017, **53**, 9994-9997.